Journal of Advanced Ceramics
2024, **13**(10): 1666–1676
https://doi.org/10.26599/JAC.2024.9220968

Research Article

Flexible and resilient Co/TiO_2/SiOC nanofibers via electrospinning: Towards thermal and electromagnetic wave protection

Linghao Pan[1,2], Rui Liu[1,2], Fanqi Meng[1,2], Zhonglin Li[1,2], Yi Hou[1,2]✉, Lixi Wang[1,2]✉

[1] *College of Materials Science and Engineering, Nanjing Tech University, Nanjing 211816, China*
[2] *Jiangsu Collaborative Innovation Center for Advanced Inorganic Function Composites, Nanjing 211816, China*

Received: July 4, 2024; Revised: September 3, 2024; Accepted: September 7, 2024

Abstract: Polymer-derived ceramic (PDC)-SiOC is a highly promising microwave-absorbing material characterized by high temperature resistance, lightweight, high strength, and extremely low cost. The weak electromagnetic wave (EMW) attenuation capacity and poor flexibility of single precursor-derived SiOC ceramics significantly limit their further application. This study employs a simple electrospinning technique to uniformly distribute Co and TiO_2 within amorphous SiOC nanofibers. The three-dimensional porous structure formed by continuous nanofibers endows Co/TiO_2/SiOCs with high porosity, significantly reducing the thermal conductivity and enhancing the conductive loss of electromagnetic waves within the nanofiber mats. Additionally, the introduction of Co and Ti promotes nanostructuring of the fibers and introduces polarization interfaces and defects, thereby enhancing the polarization loss of the samples. With a filler content of only 5 wt%, the Co/TiO_2/SiOC sample heat-treated at 800 °C (in silicone resin) exhibits an effective absorption bandwidth (EAB) of up to 8.64 GHz (9.36–18.00 GHz) at a thickness of 3.25 mm, achieving a minimum reflection loss (RL_{min}) value of −66.00 dB at 17.11 GHz with a matching thickness of 2.50 mm. Moreover, the nanofiber mats also demonstrate excellent thermal insulation performance (thermal conductivity ranging < 0.041 $W \cdot m^{-1} \cdot k^{-1}$), remarkable flexibility (the resistance change rate after 1500 cycles of 180° bending test is less than 4%), and impressive resilience performance (residual strain < 12% after 500 cycles under 60% strain conditions). The successful preparation of such multi-functional nanofiber mats is promising for the application of thermal and microwave protection.

Keywords: SiOC nanofibers; electrospinning; microwave absorption; thermal insulation; flexibility and resilience

1 Introduction

Rapid advancements in the electronics industry have provided significant convenience to the civilian uses but have also contributed to electromagnetic pollution, posing risks to human safety [1,2]. To meet the diverse requirements of civilian applications, such as devices with varied curved surfaces and clothing for different working environments, electromagnetic wave (EMW) absorbers must not only provide effective absorption but also be lightweight, easily processed, and sufficiently flexible [3,4]. Additionally, EMW-absorbing materials face challenges under extreme conditions commonly encountered in construction and transportation industries, including high temperatures, frequent vibrations, and pressure impacts [5,6]. Hence, exploring materials with admirable thermal insulation, remarkable flexibility and resilience, superb processability, and ultra-lightweight characteristics represents the development trend of multifunctional EMW absorbers [7–10].

Polymer-derived ceramics (PDCs) have broad prospects for development as high-temperature EMW absorbers [11]. PDC-SiOC is particularly attractive owing to its robust mechanical properties and high-temperature resistance in extreme environments, as well as its low density, high strength, and low raw material cost. These features highlight its impressive potential for applications in the field of high-temperature, lightweight multifunctional absorbing materials [12,13]. Nevertheless, SiOC ceramics derived from a single precursor polymer exhibit poor EMW absorption performance due to their low dielectric properties. To improve EMW attenuation performance, it is common to introduce a second phase into the SiOC matrix, leveraging the advantages of various components to enhance the EMW absorption [14]. The introduction of SiOC-based composite materials with high dielectric loss phases (such as n-SiC/SiOC ceramics [15], C/SiOC nanocomposites [16], SiC nanowires/SiOC [17], SiC nanowires/C/amorphous SiOC composite ceramic materials [18], and one-dimensional (1D) nanostructures/SiOC ceramics [19]) has been reported to optimize impedance matching with free space and improve microwave dissipation, thereby enhancing EMW absorption performance. Additionally, magnetic materials are also promising. For instance, the introduction of Fe source involving ferrocene [20], tetrabutyl titanate [21], and Sc_2O_3 [22] has been reported to improve the crystallinity and magnetic loss of SiOC ceramics. In addition, the incorporation of multiphase structures (such as Co_2Si@SiOC/Co_3O_4 [23], Fe_xSi_y/SiC@SiOC [24], and carbon nanotube (CNT)/CoSi/SiOC [25]) has improved the dielectric properties.

On the other hand, the inherent brittleness of SiOC ceramics severely hinders their use in complex environments [26]. Researchers have adopted strategies such as microcrack

✉ Corresponding authors.
E-mail: Y. Hou, houyi@njtech.edu.cn;
L. Wang, wanglixi_njut@163.com

toughening, phase transition toughening, and whisker toughening to prepare flexible ceramic films or membranes that can withstand some degree of bending. However, these approaches have difficulty in releasing external stress under large bending deformation, resulting in limited improvement in flexibility. Compared with films or sheets, 1D ceramic nanofibers possess a higher aspect ratio and gratifying continuity, which help to withstand large deformation and enhance the flexibility. Moreover, the fibrous structure could further create abundant interfaces and conductive networks to improve the EMW absorption efficiency [27]. Nanofibers of SiC and SiO_2 (such as Co/SiC [28], Fe_3Si/SiC [29], ZrC/SiC [30], HfC/SiC [31], PIP–SiC/SiC [32], C–SiC [33], ZrO_2/SiC [34], PVDF/SiC/$FeCl_3$ [35], SiC@SiO_2/carbon [36], PAN/SiO_2–TiO_2–NH_2 [37], and PVC/SiO_2/SiO_2@Ag [38]) have improved mechanical properties substantially. However, breakthroughs are still needed to optimize the EMW absorption performance and mechanical properties (flexibility, compressive strength, and thermal insulation performance) of SiOC nanofibers.

In this case, electrospinning is a versatile method for producing 1D micro-nanofiber materials with uniform size distribution and consistent morphology. Examples of nanofibers successfully prepared by electrospinning include TiO_2/Co/carbon nanofiber (CNF) nanocomposites [39], SiO_2 [40], ZrO_2 [41], graphene nanofibers [42], and CoO_x/C [43]. 1D fibers obtained through electrospinning exhibit high anisotropy and conductivity, significantly enhancing the microwave attenuation capability [44,45]. Moreover, precise control of fiber diameter and microstructure can be achieved by adjusting process parameters, providing greater flexibility in the preparation process. To improve both the flexibility and EMW absorption performance, the strategy of multi-phase composition could be applied in the electrospinning process of SiOC nanofibers. Co is renowned as a ferromagnetic material widely used for microwave attenuation. Owing to its natural resonance, Co exhibits significant magnetic loss at high frequencies, improving attenuation efficiency [46]. Among numerous dielectric materials, TiO_2, a widely studied n-type semiconductor material, exhibits excellent dielectric loss performance [47]. Xia *et al.* [48] synthesized hydrogenated TiO_2 nanocrystals, and their enhanced performance was attributed to significant polarization under EMW activation. Qiao *et al.* [39] also demonstrated that introducing the TiO_2 phase can significantly enhance the EMW absorption intensity without affecting the maximum effective absorption bandwidth (EAB).

Herein, Co and TiO_2-modified SiOC nanofibers were innovatively synthesized using a straightforward and controllable electrospinning technique, which resulted in an excellent three-dimensional (3D) continuous network structure and a homogeneous distribution of composites within the fibers. The introduction of Co and Ti elements improved the spinnability of the solution and facilitated the nanonization of the fibers. This staggered composite network significantly enhanced the EMW absorption with a filler content of merely 5 wt%, covering the EAB of 8.64 GHz with a thin thickness. The 1D and nano-dimensionall fibers guarantee the flexibility, compressive resistance, and thermal insulation properties of Co/TiO_2/SiOCs.

2 Experimental

2.1 Fabrication of modified SiOC fibers

The preparation process consists of two steps. First, the SiOC precursor solution, which was a mixture of 0.9 g of polyvinylpyrrolidone (PVP, Shanghai Macklin Biochemical Co., Ltd., China, number-average molecular weight (M_n) = 1,300,000), 12 mL isopropanol, 2 mL N,N-dimethylformamide (DMF, Shanghai Aladdin Bio-chem Technology Co., Ltd., China), and 1.8 g of poly(methylsilsesquioxane) (MK, Kestro Co., Ltd., China, average M_n = 2500) as the precursor, was stirred for 1 h until it was completely dissolved. Further, 0.06 g dibutyltin dilaurate (Nanjing WANQING chemical Glass ware & Instrument Co., Ltd., China) as a catalyst, 0.27 g of cobalt(III) acetylacetonate ($Co(acac)_3$, Shanghai Macklin Biochemical Co., Ltd., China), and 0.72 g titanium acetylacetonate ($TiO(acac)_2$, Shanghai Macklin Biochemical Co., Ltd., China) were added to the solution. The mixture was stirred for 3 h to form a homogeneous MK precursor solution. Subsequently, the precursor solution was transferred into a 10 mL plastic syringe without a plunger for electrospinning. During the electrospinning process, a stainless steel needle (with an inner diameter of approximately 0.62 mm) was connected to the syringe, which was pumped at a flow rate of 0.03 mL·min^{-1}, and a positive voltage of 15 kV was applied to the needle. The as-spun MK precursor nanofibers were collected by a low-speed roller rotating at 150 r/min with an applied negative voltage of 5 kV. The distance between the tip of the needle and the roller collector was 14 cm. At this stage, the modified SiOC precursor nanofibers were prepared. Second, the modified SiOC precursor nanofibers were cured at 190 °C in air for 1 h at a heating rate of 5 °C·min^{-1}. The cured nanofiber mats were pyrolyzed at a rate of 2.5 °C·min^{-1} to 700/800/900 °C in an Ar atmosphere and then held at the target temperature for 2 h (samples were labeled as CTS-700/800/900).

2.2 Characterization

The morphology and microstructure of the samples were captured by a scanning electron microscope (SEM; S-4700, Hitachi, 15 kV) and a transmission electron microscope (TEM; F-30, FEI-Tecnai, 300 kV). An X-ray diffractometer (XRD; Rigaku Ultima IV with Cu Kα radiation), a Modular Raman Microscope (Jobin Yvon, HORIBA; laser source wavelength of 514 nm), and an X-ray photoelectron spectrometer (XPS; ESCALAB 250Xi, Thermo Fisher) were used to obtain the crystal structure, Raman spectra, and chemical structure. Static electrical conductivity of the modified SiOC nanofibers was determined by using a direct current resistance tester (6220, Keithley) with a four-probe method. The mechanical compression properties were tested by using an Instron 5500 universal testing machine. To measure the microwave absorption properties, 5.0 wt% SiOC nanofibers (3 layers) were mixed with silicone resin, and toroid-shaped composite samples (outer toroidal diameter (D_{out}) = 7.0 mm, inner toroidal diameter (D_{in}) = 3.0 mm) were prepared with our self-made stamping die mold. Complex permeability and permittivity of the composites were tested in APC7 coaxial line mode with an Agilent HP8722D vector network analyzer by measuring the reflection coefficient S_{11} and the transmission coefficient S_{21}.

3 Results and discussion

3.1 Phase composition and microstructure of samples

The synthetic process for modified SiOC fibers is displayed in Fig. 1(a). CTSs exhibit phenomenal compressive and flexibility properties, as represented in Figs. 1(b) and 1(c). Additionally, the free-shaping capability of CTSs allows them to adapt to various macrostructures for specific application scenarios (Fig. 1(d)). The

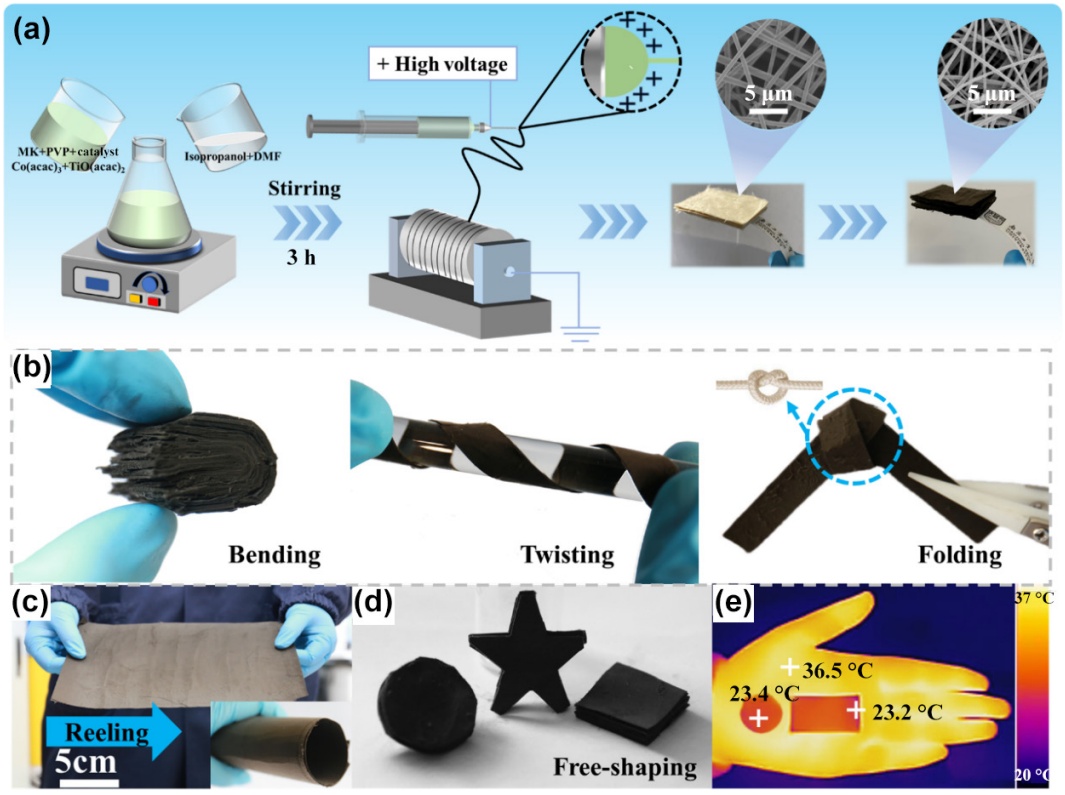

Fig. 1 (a) Schematic illustrations for preparation route of CTSs. (b) Flexible demonstration of CTS-800. Digital photographs showing (c) whole fiber mat after heat treatment and (d) free-shaping macrostructure. (e) Infrared thermal image of the CTS-800 composites.

infrared thermal image (Fig. 1(e)) illustrates the reduced thermal radiation difference between the hand and the samples. These excellent performances can be attributed to the unique microstructure of CTSs [44].

The SEM image in Fig. S1 in the Electronic Supplementary Material (ESM) illustrates the discontinuity of pure SiOC fibers with an average diameter of approximately 1.17 μm. Figures 2(a2)–2(a4) show SEM images of CTSs, which consisted of intertwined SiOC nanofibers. A large number of uniformly and randomly distributed nanofibers, with diameters of 400–800 nm (Fig. S1 in the ESM), overlap to form a three-dimensional micro-network structure. This fiber-to-fiber distribution significantly facilitates structural integrity and maximizes flexibility and thermal insulation. Additionally, the rough and wrinkled morphology increases the specific surface area, providing more active sites that promote the loss of EMW [49]. The high-resolution transmission electron microscopy (HRTEM) images display the nanocrystal-attached SiOC nanofibers (Fig. 2(b)), in which the observed interplanar spacings of selected lattice stripes are 0.20 and 0.35 nm, which can be attributed to the (100) plane of Co crystal particles and the (101) plane of TiO_2, respectively (Fig. 2(d)). Additionally, the HRTEM and selected area electron diffraction (SAED) images of the SiOC nanofiber matrix indicate that no lattice fringes are present in the matrix, suggesting the presence of amorphous SiOC (Figs. 2(c) and 2(d)). Furthermore, the EDS mapping images of CTS-800 also exhibit that all the elements (Co, Ti, Si, O, and C) are uniformly distributed on the surface of the composite nanofibers (Fig. 2(e)), corresponding with the TEM results.

The nanosizing of SiOC fibers mainly contributes to the optimization of the electrospinning solution, whose viscosity and conductivity were investigated and are shown in Fig. 2(f). After the addition of the precursor MK, the viscosity of the precursor solution significantly accumulates to 160 mPa·s, while the conductivity of the solution significantly drops. With the addition of the composite materials $TiO(acac)_2$ and $Co(acac)_3$, the viscosity of the solution decreases almost linearly from 160 to 88 mPa·s, whereas the conductivity rapidly increases to 1.71 μs·m^{-1}. At relatively lower viscosities, the entanglement of polymer molecular chains decreases, making electrospinning to form nanofibers easier. On the other hand, the enhanced conductivity simultaneously heightens the spinnability of the electrospinning precursor solution. Consequently, the augmented charge on the electrospinning jet promotes stretching, leading to the formation of more uniform and nanoscale fibers [50].

The XRD peak images of SiOC-800 and CTS-700/800/900 (Fig. 2(g) and Fig. S2 in the ESM) reveal a broad peak between 15° and 35°, indicative of amorphous SiOC. Additionally, a weak peak at 41.7° corresponds to the (100) reflection of hexagonal close-packed Co (JCPDS No. 89-4308), while the peak at 53.9° is attributed to the (105) plane of anatase TiO_2 (JCPDS No. 21-1272) [51]. The images suggest that SiOC, TiO_2, and Co in the prepared samples are essentially amorphous structures with relatively low crystallinity [52]. This agrees with the results of TEM and SAED, which reveal amorphous microstructures.

The degree of graphitization is a crucial parameter of amorphous carbon derived from organic components, directly determining its conductivity [53]. The electrical conductivity of EMW absorbing materials should be controlled within an appropriate range to ensure sufficient conduction loss while avoiding EMW reflection caused by excessive electrical conductivity [54]. Figure 2(h) presents the Raman results of the prepared CTSs (mixed Gauss-Lorentz fit of the D-band and G-band for CTSs shown in Fig. S3 in the ESM). The D band at ~1350 cm^{-1} is attributed to the disordered structure caused by carbon vacancies, amorphous carbon species, and lattice defects,

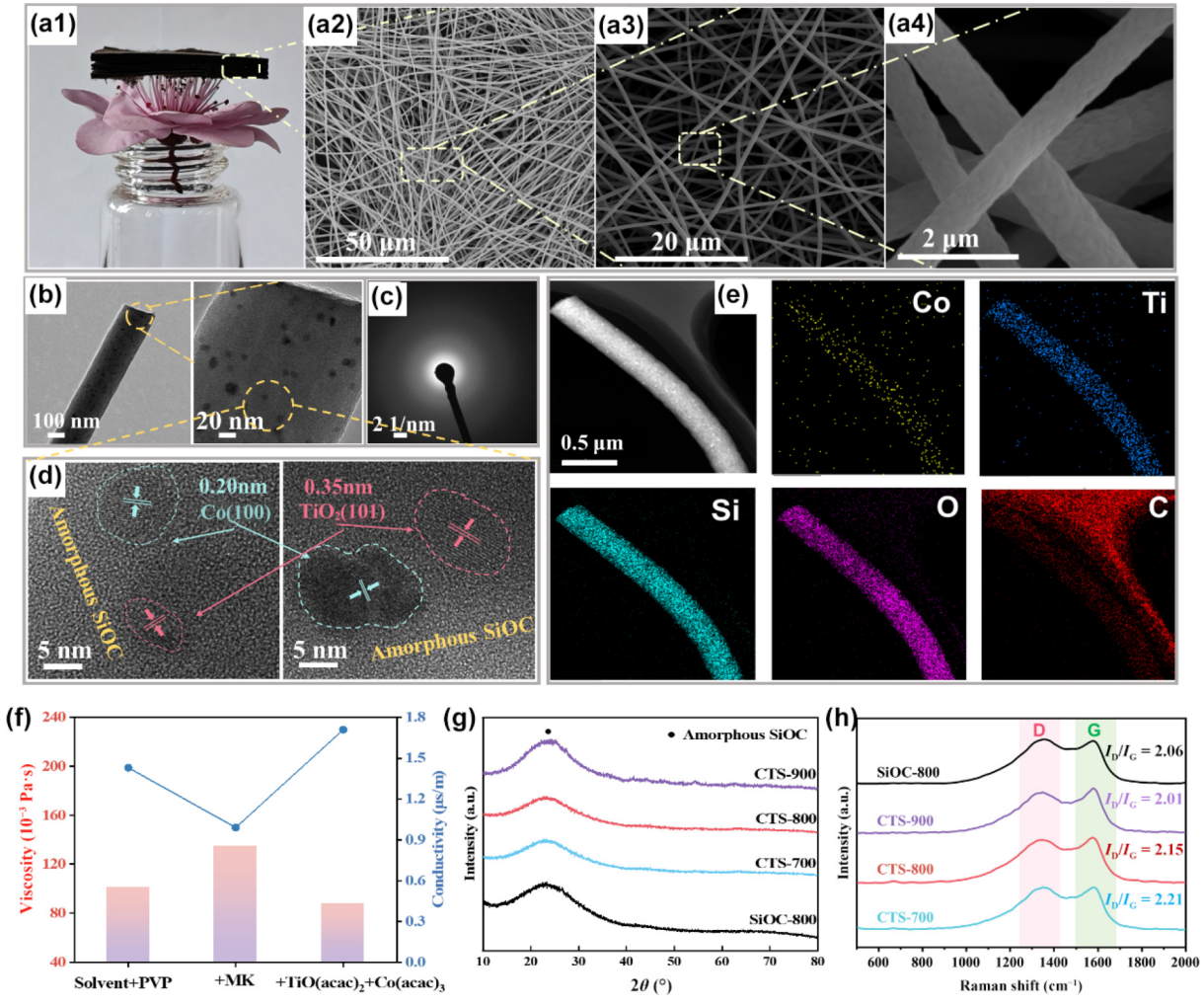

Fig. 2 (a1) Digital image of CTS-800. SEM images of (a2–a4) random distribution and rough surface microstructure; (b) TEM images and (c) SAED pattern of single CTS-800 nanofiber; (d) HR-TEM image of corresponding region in (b); (e) coincident EDS elemental maps; (f) effects of addition of precursors or complexes on viscosity and conductivity of electrospinning solution; (g) XRD patterns of pure SiOC-800 and CTSs at various thermal treatment temperatures; (h) Raman spectra of SiOC-800 and CTSs.

while the G band at ~1590 cm^{-1} is associated with graphitic carbon. The intensity ratio of the D band to the G band (I_D/I_G) represents the degree of disorder [55] and the level of graphitization in the carbon structure [56]. The I_D/I_G ratios of CTSs exhibit the opposite trend (from 2.21 to 2.01) with the rising of heat treatment temperature. During the heat treatment of SiOC-800 and CTSs, the carbothermal reduction reaction promotes the conversion of free carbon in the nanofibers into graphite carbon, thereby enhancing the graphitization of the samples. The Raman spectroscopy results indicate that the graphitization degree of the samples increases with increasing heat treatment temperature.

The surface chemical composition of the CTS-800 nanofibers was analyzed by via XPS. The wide-scan XPS spectra (Fig. S4 in the ESM) confirmed the presence of Co, Ti, Si, C, and O elements. Table S1 in the ESM summarizes the contents of Co, Ti, Si, C, and O in the CTS-800 nanofibers. In the Si 2p spectra, the presence of Si–O–C bond (corresponding to the peak at 102.1 eV) confirms the generation of amorphous SiOC, with additional peaks at 102.9 and 103.6 eV corresponding to Si–O and O–Si–O units, respectively, which verify the existence of SiO_x phase. The Co 2p spectrum shows two characteristic peaks centered at 782.0 and 796.0 eV, corresponding to Co $2p_{3/2}$ and Co $2p_{1/2}$, respectively. The peak at 777.9 eV can be attributed to metallic Co, while the peaks at 780.2 and 783.6 eV are attributed to the presence of Co^{2+} and Co^{3+}. In the Ti 2p spectra, both rutile TiO_2 phases (crystalline Ti^{4+}, 459.1 and 465.0 eV) and disordered or low-crystalline TiO_x (amorphous Ti^{4+}, 458.5 and 464.0 eV) are present in the CTS-800 nanocomposites, while CTS-800 also contains incompletely oxidized Ti^{2+} (456.2 and 462.0 eV) [57]. The XPS results also corroborate the uniform distribution of Co and TiO_2 nanocrystals in the SiOC fibers, which is in accordance with the results from TEM and XRD.

3.2 EMW absorption performance

To evaluate the EMW absorption performance of SiOC-800 and CTSs, the dielectric electromagnetic (EM) parameters ($\varepsilon_r = \varepsilon' + j\varepsilon''$) were investigated, and the results are depicted in Fig. 3(a). The ε' and ε'' of SiOC-800 remain consistently low in the frequency range of 2–18 GHz. As the heat treatment temperature rises, both ε' and ε'' of CTSs tend to increase from CTS-700 to CTS-900. According to Debye theory, ε' represents the storage capability of electricity, while ε'' represents the loss capability of the medium (Eqs. (1) and (2)) [10,47]:

$$\varepsilon' = \varepsilon_\infty + \frac{\varepsilon_s - \varepsilon_\infty}{1 + \omega^2\tau^2} \quad (1)$$

$$\varepsilon'' = \omega\tau\frac{\varepsilon_s - \varepsilon_\infty}{1 + \omega^2\tau^2} + \frac{\sigma}{\varepsilon_0\omega} = \varepsilon_p'' + \varepsilon_c'' \quad (2)$$

where ε_s represents the stationary frequency dielectric constant; ε_∞ represents the infinite frequency dielectric constant; ε_0 represents the permittivity of free space; ω, τ, and σ represent the angular frequency, polarization relaxation time, and conductivity, respectively; ε_p'' and ε_c'' represent the abilities of polarization loss and conduction loss, respectively.

ε'' depends on both ε_c'' and ε_p''. As shown in the inset of Fig. 3(a), the addition of second-phase materials (Co and Ti) promotes the nanostructuring and continuity of the fibers, whereas increasing the processing temperature of CTS samples enhances the carbon content in the nanofibers. These factors facilitate electron transfer within the fibers, resulting in low conductivity for SiOC-800 and increased conductivity for CTS samples as the heat treatment temperature rises. As shown in Fig. S5 in the ESM, ε_p'' significantly increases and then steadily drops, varying within a narrow range as the frequency increases. Moreover, the evolution of ε_c'' aligns with that of ε''. The contribution of ε_c'' to ε'' is significantly higher than that of ε_p'', indicating that the primary factor in the EMW attenuation of CTSs is conductive loss.

Additionally, the higher carbon content accelerates the electron transfer rate (Table S1 in the ESM), resulting in a significant increase in electrical conductivity and potentially increasing the conductive loss [5]. As the degree of graphitization in the samples increases, the amorphous phase in the nanofibers decreases, further improving the dielectric performance. Owing to the large aspect ratio of nanofibers, induced polarization charges are easily formed at both ends of each CTS [58]. Under a periodically alternating electromagnetic field, polar molecules or functional groups periodically rotate and rearrange, leading to dipole loss [59]. Additionally, owing to the different dielectric properties of SiOC, TiO_2, and Co, the abundant non-uniform interfaces caused by their disordered arrangement dramatically promote the accumulation and rearrangement of local charges [60], resulting in interface polarization, thereby significantly increasing the value of ε'' and enhancing the dielectric loss [61,62]. Figures 3(b) and 3(c) present the dielectric loss and magnetic loss capabilities of all the samples. Since the μ' values are close to 1 and the $\tan\delta_\mu$ values are almost zero, dielectric loss should be the dominant factor [63]. Moreover, $\tan\delta_\varepsilon$ reflects the inherent dissipation capability of dielectric materials [44], which exhibits an escalatory trend from SiOC-800 to CTSs, further confirming the increased dielectric loss capability of CTSs.

Specifically, the attenuation constant (α) reflects the attenuation ability of the absorbing material to absorb internal EMW [64] (as shown in Methods in the ESM). Figure 3(d) depicts the variation in α for samples from 2 to 18 GHz, which reveals a positive correlation between α and the heat treatment temperature. Moreover, the values of α increase with frequency, indicating the excellent EMW attenuation capability of the samples at high frequencies. The larger the attenuation coefficient, the greater the potential for excellent performance in EMW absorption [65].

However, a suitable ε' value is an important criterion for an ideal absorber. An excessively large ε' value may result in the reflection of most EMW from the surface of the absorber layer. Conversely, EMWs are prone to penetrate the coating, which is unfavorable for EMW attenuation [61]. Similarly, excessively high

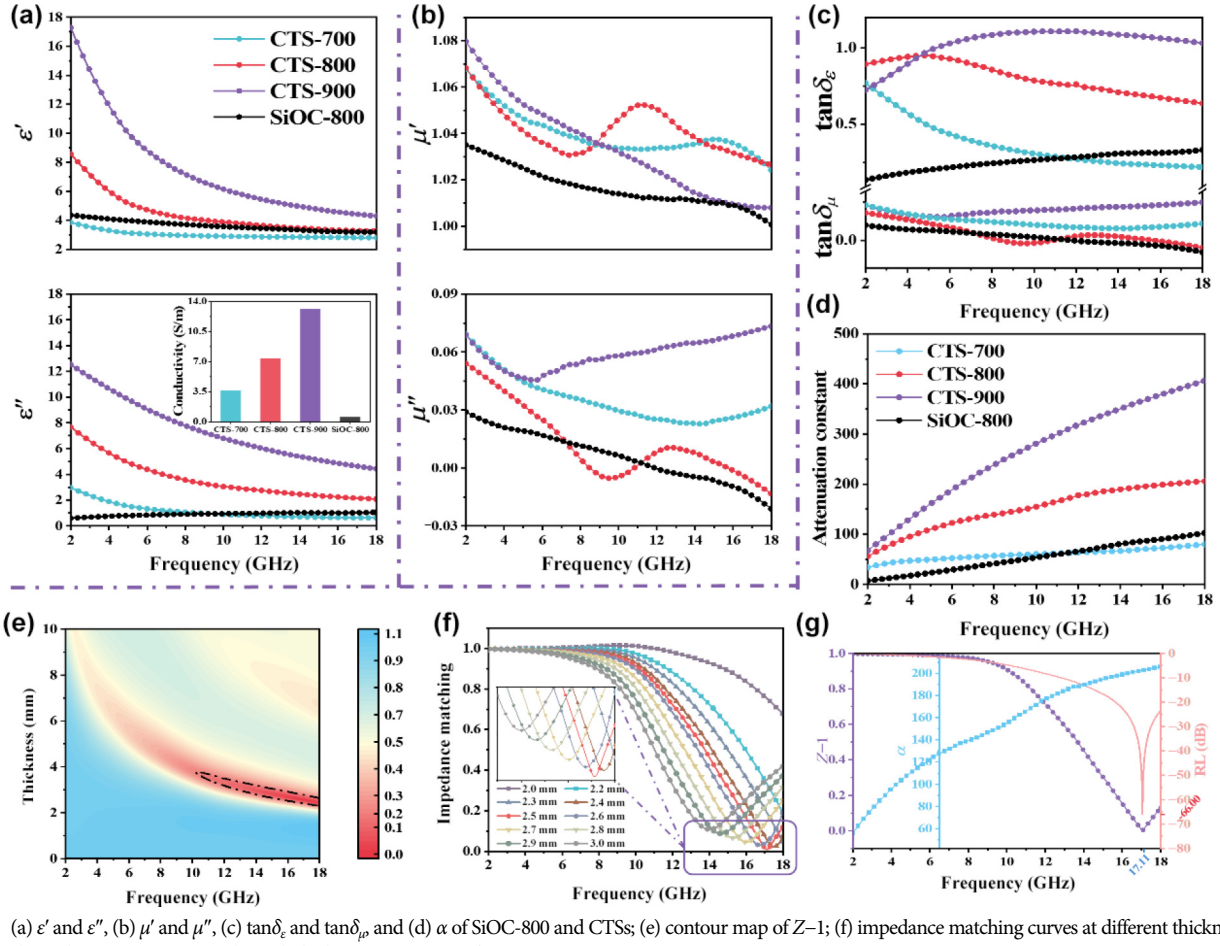

Fig. 3 (a) ε' and ε'', (b) μ' and μ'', (c) $\tan\delta_\varepsilon$ and $\tan\delta_\mu$, and (d) α of SiOC-800 and CTSs; (e) contour map of $Z-1$; (f) impedance matching curves at different thicknesses; (g) correlation between RL, $Z-1$, and α with thickness at 2.50 mm of CTS-800.

ε'' values may result in impedance mismatch, impairing the EMW absorption capability. Therefore, moderate dielectric performance is crucial in the design of absorbing materials, aiming to achieve optimal attenuation and matching [66]. The impedance matching characteristic ($|Z_{in}/Z_0|$ (Z)) determines whether the EMW projected onto the material surface can effectively enter the interior of the material or be reflected back to free space again [67]. The values of Z_{in} and Z_0 are explained in Methods in the ESM [68]. The contour maps of Z–1 for SiOC-800 and CTSs are presented in Fig. S6 in the ESM and Fig. 3(e). Except for the CTS-800, all the samples exhibit indifferent Z–1 values across the frequency range, indicating that CTS-800 will ultimately generate a wider effective absorption region. Figures 3(f) and 3(g) and Fig. S7 in the ESM show that CTS-800 achieves optimal impedance matching at the thickness of 2.50 mm, coupled with an excellent attenuation constant, and that the absorber has a minimum reflection loss value of −66.00 dB at the frequency of 17.11 GHz. In summary, the excellent microwave absorption performance of the CTS-800 nanofiber mats mainly originates from the optimal EMW attenuation ability and appropriate impedance matching.

Reflection loss (RL) is a critical factor in evaluating the EMW absorption performance of CTSs [69] (as shown in Methods in the ESM). As a fantastic microwave absorber, a low filling rate is one of the key judgment indicators [59]. In this experiment, the microwave absorption performance of the samples was systematically analyzed at a super low filling rate of 5 wt%. As shown in Figs. S8(a)–S8(d) in the ESM, the difference in the absorption intensity of the samples can be intuitively demonstrated. A comparison of the data in Figs. 4(a)–4(d) reveals that the RL_{min} of SiOC-800 reaches −25.10 dB, with an EAB_{max} of 4.33 GHz at a thickness of 8.22 mm. With the introduction of Co and TiO_2, the fiber continuity of CTSs is enhanced, and the rough surface morphology and micro-network structure can effectively amplify the multiple scattering effect, further enhancing the attenuation capability of the EMW [70]. As shown in Figs. 4(c) and 4(e), the EAB_{max} for CTS-800 can reach as high as 8.64 GHz, corresponding to a frequency range of 9.36–18.00 GHz at a thickness of 3.25 mm. In contrast, the RL_{min} values of CTS-700 and CTS-900 are only −41.80 and −11.50 dB, corresponding to frequencies of 13.4 and 18.0 GHz, respectively, indicating that their absorption rates are low across the entire measurement

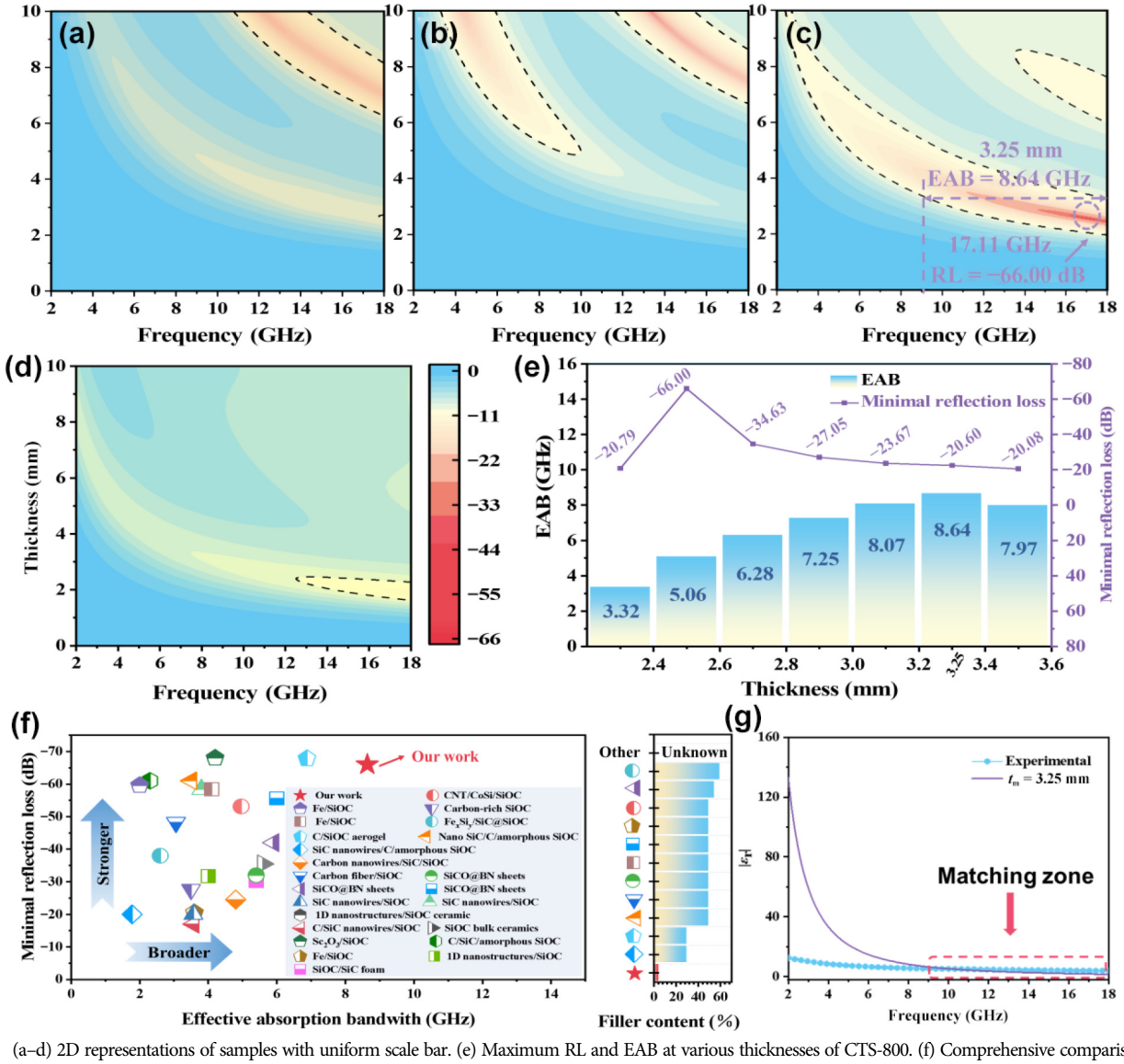

Fig. 4 (a–d) 2D representations of samples with uniform scale bar. (e) Maximum RL and EAB at various thicknesses of CTS-800. (f) Comprehensive comparison of microwave absorption performance (2–18 GHz) in terms of RL_{min}, EAB, and filler content with those of reported microwave absorbers. (g) Comparison of $|\varepsilon_r|$ curves of CTS-800 and simulated curve at t_m = 3.25 mm.

清華大学出版社 Tsinghua University Press | SciOpen

range. By comparison, CTS-800 exhibits the best EMW loss capability (Fig. S9 and Table S2 in the ESM). To further highlight the excellent microwave absorption performance of CTS-800, Fig. 4(f) and Table S3 in the ESM compare the RL_{min} and EAB_{max} of previously reported SiOC-based composite material absorbers (the relevant references are shown in the ESM). CTS-800 in our work clearly exhibits superior microwave absorption performance. The excellent EM absorption performance primarily originates from the ideal dielectric attenuation and continuous fiber structure. Owing to the precise control of the heat treatment temperature of the nanofiber mats, the optimized CTS-800 exhibits appropriate dielectric loss and impedance matching. Furthermore, the continuous network endows the fiber mat with a highly efficient microwave absorption structure. Furthermore, the loading rate of CTS-800 is significantly lower than those of other competitors. Such a low filling ratio is beneficial for both efficient attenuation and lightweight characteristics [71].

According to the context of quarter-wavelength matching model ($\lambda/4$) [72], Fig. 4(g) displays the comparison between the experimental curve obtained for CTS-800 and the theoretical curve generated by the equation for t_m = 3.25 mm. The frequency range aligns closely with the EAB range of the 2D mapping image of RL in Fig. 4(c), from 9.36 to 18.00 GHz (for a sample thickness of 3.25 mm). From the obtained results, we can infer that the region of EAB in Fig. 4(g) corresponds to the extinction condition of $\lambda/4$ (thin thickness region).

3.3 Resilient compression performance

We investigated the compressibility of laminated CTS-800 using a universal testing machine. The stress–strain (σ–ε) curves of CTS-800 under various compressive strains (30%–70%) are plotted, as shown in Fig. 5(a). Curves at different strains form closed loops, indicating excellent compressive recovery ability. The maximum compressive stress of CTS-800 sample at 70% strain approximately attains to 18 kPa, indicating its ability to withstand thousands of times its weight without structural damage [73]. The first stage of the loading process is due to the discontinuous structure between multilayer nanofibers, allowing the nanofibers enough space to deform at lower compressive strains. Subsequently, the number of bent nanofibers accumulates, and the stress gradually transfers to the reinforced bonding points, resulting in an increasing stress. Finally, owing to the densification of the overall structure, under applied stress, the contact points between multilayer nanofibers significantly increase, leading to a sharp increase in stress [74]. Figure S10 in the ESM demonstrates that the σ–ε curves remain constant within the testing speed range of 5–60 mm·min^{-1}. Additionally, the CTS-800 nanofibers exhibit stable resilience and long-term cyclic compression durability. A total of 500 cycles of fatigue tests were conducted at a strain of 60% (Fig. 5(b)), and the corresponding σ–ε curves maintain closed-loop shapes, indicating a consistent rebound behavior. At the 500th cycle, the maximum stress remains above 92% of the value at the 1st cycle, and the energy loss coefficient is approximately 0.3

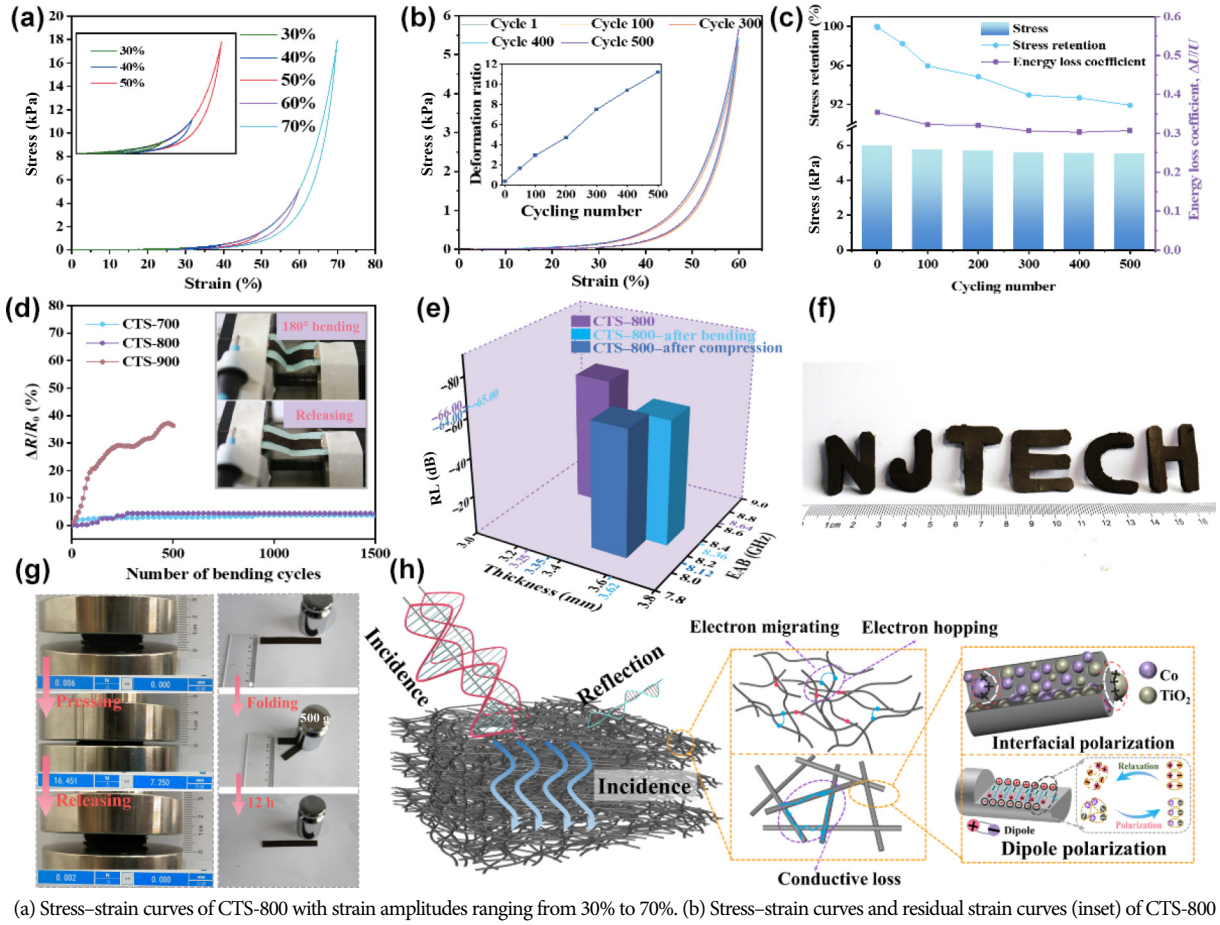

Fig. 5 (a) Stress–strain curves of CTS-800 with strain amplitudes ranging from 30% to 70%. (b) Stress–strain curves and residual strain curves (inset) of CTS-800 for up to 500 compressive cycles (strain = 60%). (c) Stress retention and energy loss coefficient of CTS-800 as a function of number of compressive cycles (strain = 60%). (d) Resistance change rate of CTSs under cyclic 180° bending test (the inset shows digital photos of CTSs under 180° bending experiments). (e) Comparison of microwave absorption performance of CTS-800 before and after tests of bending for 1500 times/compression for 500 times. Digital photographs of (f) tailorable performance and (g) compressive and flexural performance of CTS-800. (h) Schematic diagram of EMW absorption characteristics of CTSs.

(Fig. 5(c)). These conclusions demonstrate the excellent compressive durability of CTS-800.

To characterize the bending resistance of the flexible pads, the resistance change rate ($\Delta R/R_0$) of CTS-800 is presented in Fig. 5(d) and Fig. S11 in the ESM, where ΔR represents the resistance change and R_0 denotes the initial resistance. The testing process is shown in Fig. S12 in the ESM (0–3 bending tests and real-time monitoring videos can be found in Video S1 in the ESM). The dynamic resistance during repeated bending at 180° was recorded using a double-probe method. The CTS-700 and CTS-800 mats exhibit excellent reliability and durability. After 1500 bends, as the resistance change rate remains less than 5%, no significant resistance change occurs, indicating that the microstructures of CTS-700 and CTS-800 remain relatively intact throughout the experimental process. For CTS-900, the resistance increases by approximately 20% after 100 cycles, indicating a significant shrinkage in reliability. However, owing to the wide diameter of the SiOC-800 fibers and the presence of numerous broken fibers, the fiber membrane is inherently brittle, making it unsuitable for bending tests (Fig. S13 in the ESM). In contrast, the admirable flexibility of CTS-700 and CTS-800 can be attributed to the size effect of 1D nanofiber materials. When determining the fiber composition, the one-dimensionalization and nanosizing of fibers constitute another factor affecting the bending stiffness of the nanofiber mats. Reducing the fiber size aids in reducing the number of macroscopic defects and improving the overall uniformity of ceramic fiber materials, providing more free surfaces to release stress, thereby demonstrating the excellent flexibility of nanofibers [75].

To further assess the reliability of CTS-800, the EMW absorption performance was measured after bending for 1500 times and after 500 cycles of compression at a strain of 60% (Fig. 5(e)). The ε' and ε'' values of CTS-800 decrease, which can be attributed to the decrease in conductivity [44] (Fig. S14 in the ESM). Furthermore, at a frequency of 9.90 GHz, the RL_{min} of the bent CTS-800 nanofiber mat slightly drops to −65.00 dB, while the RL_{min} of the compressed nanofibers declines to −64.00 dB at a frequency of 10.94 GHz, indicating good reliability. When the thickness is 3.62 mm, the EAB of bent CTS-800 slightly decreases to 8.36 GHz, and the compression is 8.12 GHz at a thickness of 3.62 mm. The attenuation in the EMW absorption performance of bent and compressed CTS-800 is mainly due to the decline in electrical conductivity caused by the fracture of the internal 3D conductive network of the mat. However, the fractured fibers may generate more interfaces, resulting in reflection and scattering of incident microwaves [44]. Therefore, while adapting to potential applications (Figs. 5(f) and 5(g)), even after long-term folding and compression, the EMW energy is effectively converted into internal energy, resulting in acceptable reliability and durability.

Figure 5(h) presents the possible EMW absorption mechanism of the synthesized CTS nanofiber mats. First, multiple reflections and scattering occur. The unique larger specific surface area of 1D nanofibers facilitates the generation of multiple reflections and scattering of EMW, thereby promoting their absorption [76]. Second, there is conductive loss. Owing to the unique disordered distribution and intertwined form of CTS nanofiber mats, the resulting three-dimensional conductive network structure provides transmission channels for electron migration and hopping, effectively accelerating the rate of electron transfer [77]. Finally, polarization loss occurs. The large aspect ratio of nanofibers, combined with the rich surface defects and polar functional groups of composite materials, is conducive to the formation of polarization centers, inducing dipole polarization. Under alternating electromagnetic fields, the abundant interface between SiOC, TiO_2, and Co induces local charge accumulation and rearrangement, resulting in interface polarization [62].

3.4 Thermal insulation performance

The prepared CTSs exhibit excellent thermal stability at high temperatures, which is crucial for high-temperature EMW absorption applications. The thermal conductivity (k) of CTSs shows a range of 0.0378–0.0404 $W{\cdot}m^{-1}{\cdot}K^{-1}$ (Fig. 6(a)). Notably, the thermal conductivity of CTS-900 at room temperature is only 0.0378 $W{\cdot}m^{-1}{\cdot}K^{-1}$, indicating that the obtained nanofiber mats are excellent thermal insulators. Thermal conductivity (k) is closely related to the density (Table S4 in the ESM) of fiber materials [78], and the process for testing the density of CTSs is detailed in Methods in the ESM. To visually demonstrate the thermal insulation efficiency of CTSs, samples (Fig. 6(b)) were placed on a heating plate set at 250 °C. The relationship between their thermal infrared images and heating time was recorded to monitor the dynamic temperature changes on the surface. The experimental results show that the temperature on the surface of the samples remains almost stable at approximately 60 °C for approximately 10 min and approximately 63 °C for approximately 30 min (the apparent fluctuations could be attributed to the temperature changes in the heating plate). CTS-800 demonstrates remarkable heat resistance, as it enables a fresh flower to remain unscathed for 5 min on a metal plate subjected to an intense flame from a butane blowtorch. Conversely, a flower placed directly on the metal plate is rapidly charred within mere 90 s (Fig. 6(c)).

The schematic diagram in Fig. 6(d) illustrates effective methods to reduce the thermal conductivity, including increasing porosity between fibers to reduce solid conduction (λ_{solid}). Moreover, the low-density characteristics and interconnected framework formed by the randomly oriented fiber distribution provide infinite solid conduction pathways, significantly reducing λ_{solid}. The gaps between the nanofiber layers decrease heat convection ($\lambda_{convection}$) into the inner layers of the mat and reduce thermal radiation (λ_{rad}). Additionally, the rough surface of the nanofibers effectively introduces phonon scattering, further reducing the thermal conductivity [74]. Consequently, the CTS mats exhibit excellent thermal insulation performance.

Figure 6(e) and Table S5 in the ESM summarize the details of our work compared with various multifunctional materials (including silicon-based fiber composites, foam composites and aerogel composites) reported in the literature (respective references are listed in the ESM). The CTS-800 sample exhibits the most comprehensive multifunctional properties due to its high porosity and multilayer structure along the thickness (the porosity and cross-sectional SEM images are shown in Fig. S15 in the ESM). As shown in Fig. 6(f), EMW or thermal shock waves from the outside can be significantly attenuated. Additionally, outstanding flexibility ensures that our findings can be perfectly grappled with the deformations required in various high-demand scenarios, thus enhancing work efficiency.

4 Conclusions

1D Co/TiO_2/SiOC nanofibers with a randomly distributed and uniformly sized 3D conductive network were successfully manufactured through electrospinning and subsequent heat treatment. The obtained Co/TiO_2/SiOC sample heat-treated at 800 °C exhibitsa remarkable EMW dissipation capability, with an RL_{min} value of −66.00 dB at 2.50 mm and an EAB_{max} value of 8.64 GHz at 3.25 mm. Additionally, the flexibility, resilience, and

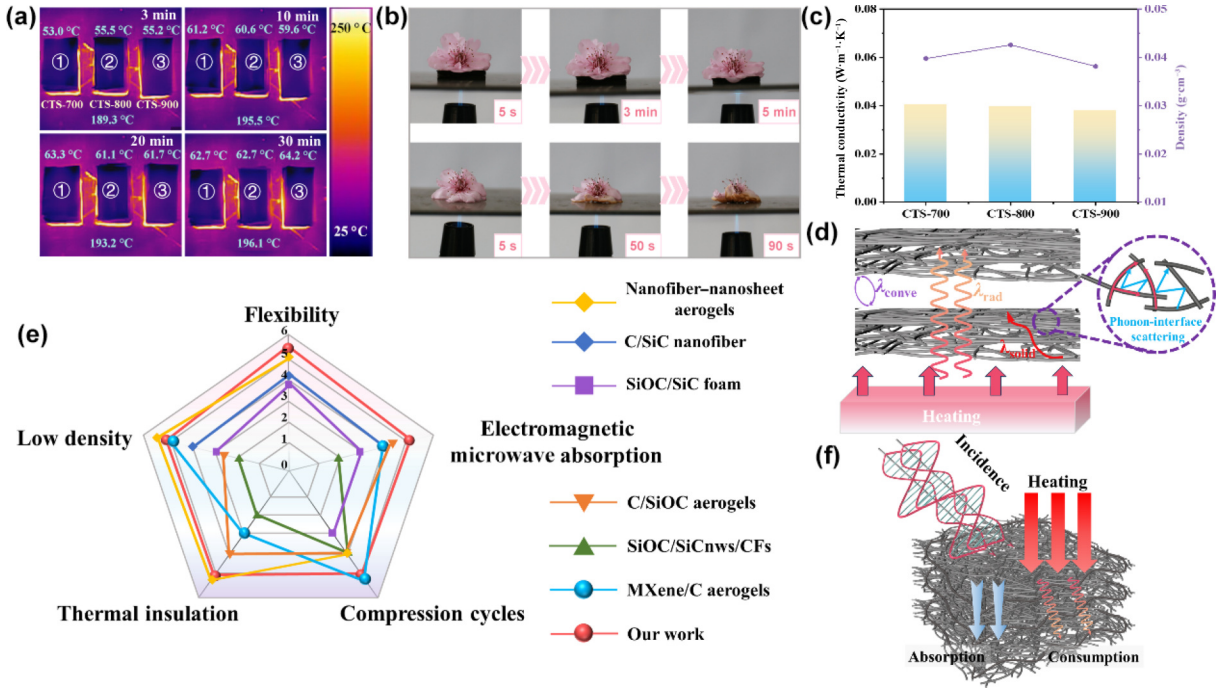

Fig. 6 Thermal insulation characteristics of CTSs. (a) Infrared images of CTSs (thickness = 10 mm) on 250 °C hot plate for 30 min. (b) Fresh flower with or without protection of CTS-800 sample under heating of butane blowtorch. (c) Thermal conductivity and porosity of CTSs and (d) schematic of thermal insulation mechanism of CTSs. (e) Radar graphic for overall appreciation of CTS-800 composite compared with mainstream multifunctional materials. (f) Schematic of CTS-800 composite microwave absorption and thermal insulation at high temperatures.

thermal insulation properties of the nanofibers are significantly enhanced. Therefore, this work overcomes the inherent brittleness of ceramic materials by optimizing the viscosity and conductivity of the spinning solution, thus pointing the way for the nanofabrication of ceramic materials and providing insights for the development of efficient EMW absorbers.

Acknowledgements

The authors thank the National Natural Science Foundation of China (General Program, No. 12374394; Youth Project, No. 52402362), Youth Project of Natural Science Foundation of Jiangsu Province (No. BK20230341), Nanjing Overseas Educated Personnel Science and Technology Innovation Program, "Qinglan Project" Young and Middle-aged Academic Leaders Program of Jiangsu Province for financial support and Priority Academic Program Development of Jiangsu Higher Education Institutions (PAPD). The computational resources generously provided by the High Performance Computing Center of Nanjing Tech University are greatly appreciated. This research was also supported by Jiangsu Students' Platform for Innovation and Entrepreneurship Training Program (No. 202410291136Y).

Declaration of competing interest

The authors have no competing interests to declare that are relevant to the content of this article.

Electronic Supplementary Material

Supplementary material is available in the online version of this article at https://doi.org/10.26599/JAC.2024.9220968.

References

[1] Wang L, Cai ZX, Su L, *et al.* Bifunctional SiC/Si_3N_4 aerogel for highly efficient electromagnetic wave absorption and thermal insulation. *J Adv Ceram* 2023, **12**: 309–320.

[2] Zhao ZH, Qing YC, Kong L, *et al.* Advancements in microwave absorption motivated by interdisciplinary research. *Adv Mater* 2024, **36**: 2304182.

[3] Zhang S, Liu XH, Jia CY, *et al.* Integration of multiple heterointerfaces in a hierarchical 0D@2D@1D structure for lightweight, flexible, and hydrophobic multifunctional electromagnetic protective fabrics. *Nano-micro Lett* 2023, **15**: 204.

[4] Lv HL, Yao YX, Li SC, *et al.* Staggered circular nanoporous graphene converts electromagnetic waves into electricity. *Nat Commun* 2023, **14**: 1982.

[5] Lv HL, Yang ZH, Wang PL, *et al.* A voltage-boosting strategy enabling a low-frequency, flexible electromagnetic wave absorption device. *Adv Mater* 2018, **30**: 1706343.

[6] Zhang X, Tian XL, Qin YT, *et al.* Conductive metal-organic frameworks with tunable dielectric properties for boosting electromagnetic wave absorption. *ACS Nano* 2023, **17**: 12510–12518.

[7] Dou LY, Yang BB, Lan S, *et al.* Nanonet-/fiber-structured flexible ceramic membrane enabling dielectric energy storage. *J Adv Ceram* 2023, **12**: 145–154.

[8] Liu XY, Zhou JM, Xue Y, *et al.* Structural engineering of hierarchical magnetic/carbon nanocomposites via *in situ* growth for high-efficient electromagnetic wave absorption. *Nano-Micro Lett* 2024, **16**: 174.

[9] Li CP, Li D, Zhang S, *et al.* Interface engineering of titanium nitride nanotube composites for excellent microwave absorption at elevated temperature. *Nano-Micro Lett* 2024, **16**: 168.

[10] Lv HL, Yao YX, Yuan MY, *et al.* Functional nanoporous graphene superlattice. *Nat Commun* 2024, **15**: 1295.

[11] Wan HJ, Liu N, Tang J, *et al.* Substrate-independent $Ti_3C_2T_x$ MXene waterborne paint for terahertz absorption and shielding. *ACS Nano* 2021, **15**: 13646–13652.

[12] Deng YM, Ren B, Jia YJ, *et al.* Layered composites made of polymer derived SiOC/ZrB_2 reinforced by ZrO_2/SiO_2 fibers with simultaneous microwave absorption and thermal insulation. *J Mater Sci Technol* 2024, **196**: 50–59.

[13] Chen C, Zeng SF, Han XC, *et al.* 3D carbon network supported porous SiOC ceramics with enhanced microwave absorption properties. *J Mater Sci Technol* 2020, **54**: 223–229.

[14] Xiao JX, Zhan BB, Qi XS, *et al.* Metal valence state modulation strategy to design core@shell hollow carbon microspheres@$MoSe_2$/MoO_x multicomponent composites for anti-corrosion and microwave absorption. *Small* 2024: 2311312.
[15] Duan WY, Yin XW, Ye F, *et al.* Synthesis and EMW absorbing properties of nano SiC modified PDC–SiOC. *J Mater Chem C* 2016, **4**: 5962–5969.
[16] Du B, He C, Qian JJ, *et al.* Electromagnetic wave absorbing properties of glucose-derived carbon-rich SiOC ceramics annealed at different temperatures. *J Am Ceram Soc* 2019, **102**: 7015–7025.
[17] Duan WY, Yin XW, Li Q, *et al.* Synthesis and microwave absorption properties of SiC nanowires reinforced SiOC ceramic. *J Eur Ceram Soc* 2014, **34**: 257–266.
[18] Liu XJ, Xue JM, Ren FY, *et al.* Enhanced microwave-absorption properties of polymer-derived SiC/SiOC composite ceramics modified by carbon nanowires. *Ceram Int* 2020, **46**: 20742–20750.
[19] Ding DH, Wang J, Xiao GQ, *et al.* Enhanced electromagnetic wave absorbing properties of Si–O–C ceramics with *in situ* formed 1D nanostructures. *Int J Appl Ceram Tec* 2020, **17**: 734–744.
[20] Duan WY, Yin XW, Luo CJ, *et al.* Microwave-absorption properties of SiOC ceramics derived from novel hyperbranched ferrocene-containing polysiloxane. *J Eur Ceram Soc* 2017, **37**: 2021–2030.
[21] Zhang Q, Ye F, Duan WY, *et al.* Dielectric and microwave absorption properties of polymer-derived TiC/SiC/SiOC multiphase ceramics in X band. *Int J Appl Ceram Tec* 2022, **19**: 1185–1194.
[22] Xue JM, Li F, Liu YQ, *et al.* *In-situ* reaction strategy toward Sc_2O_3 reinforced SiOC ceramics for enhanced microwave absorption performance. *Appl Surf Sci* 2023, **613**: 155984.
[23] Wu YF, Zhong YW, Guan Y, *et al.* Polymer-derived Co_2Si@SiC/C/SiOC/SiO_2/Co_3O_4 nanoparticles: Microstructural evolution and enhanced EM absorbing properties. *J Am Ceram Soc* 2020, **103**: 6764–6779.
[24] Zhou C, Li S, Yu ZJ. Polymer-derived Fe_xSi_y/SiC@SiOC ceramic nanocomposites with tunable microwave absorption behavior. *Int J Appl Ceram Tec* 2022, **19**: 813–827.
[25] Yu ZJ, Chen T, Du HZ, *et al.* Single-source-precursor derived SiOC ceramics with *in-situ* formed CNTs and core–shell structured CoSi@C nanoparticles towards excellent electromagnetic wave absorption properties. *J Adv Ceram* 2023, **12**: 1119–1135.
[26] Xie YS, Cheng Y, Lyu Y, *et al.* Printable, flexible ceramic fiber paper based on electrospinning. *Rare Met* 2024, **43**: 2739–2746.
[27] Peng L, Peng HR, Wang S, *et al.* One-dimensionally oriented self-assembly of ordered mesoporous nanofibers featuring tailorable mesophases via kinetic control. *Nat Commun* 2023, **14**: 8148.
[28] Hou Y, Yang Y, Deng CR, *et al.* Implications from broadband microwave absorption of metal-modified SiC fiber mats. *ACS Appl Mater Inter* 2020, **12**: 31823–31829.
[29] Hou Y, Zhang YN, Du XQ, *et al.* Flexible Fe_3Si/SiC ultrathin hybrid fiber mats with designable microwave absorption performance. *RSC Adv* 2018, **8**: 33574–33582.
[30] Hou Y, Cheng LF, Zhang YN, *et al.* High temperature electromagnetic interference shielding of lightweight and flexible ZrC/SiC nanofiber mats. *Chem Eng J* 2021, **404**: 126521.
[31] Hou Y, Cheng LF, Zhang YN, *et al.* Enhanced flexibility and microwave absorption properties of HfC/SiC nanofiber mats. *ACS Appl Mater Inter* 2018, **10**: 29876–29883.
[32] Taguchi T, Hasegawa Y, Shamoto S. Effect of carbon nanofiber dispersion on the properties of PIP-SiC/SiC composites. *J Nucl Mater* 2011, **417**: 348–352.
[33] Huo YS, Zhao K, Xu ZL, *et al.* Electrospinning synthesis of SiC/Carbon hybrid nanofibers with satisfactory electromagnetic wave absorption performance. *J Alloys Compd* 2019, **815**: 152458.
[34] Wang YD, Han C, Zheng DC, *et al.* Large-scale, flexible and high-temperature resistant ZrO_2/SiC ultrafine fibers with a radial gradient composition. *J Mater Chem A* 2014, **2**: 9607–9612.
[35] Gong ZW, Qin J, Liu D, *et al.* Flexible PVDF/SiC/$FeCl_3$ nanofiber membrane generators with synergistically enhanced piezoelectricity. *Nano Energy* 2024, **122**: 109290.
[36] Chen Y, Wang N, Jensen M, *et al.* Catalyst-free large-scale synthesis of composite SiC@SiO_2/carbon nanofiber mats by blow-spinning. *J Mater Chem C* 2019, **7**: 15233–15242.
[37] Khalil A, Aboamera NM, Nasser WS, *et al.* Photodegradation of organic dyes by PAN/SiO_2–TiO_2–NH_2 nanofiber membrane under visible light. *Sep Purif Technol* 2019, **224**: 509–514.
[38] Liu HL, Sun YM, Xu HY, *et al.* Dual-functional design of tubular polyvinyl chloride hybrid nanofiber membranes for the simultaneous oil/water separation and *in situ* catalytic degradation. *J Membr Sci* 2022, **661**: 120955.
[39] Qiao J, Zhang X, Xu DM, *et al.* Design and synthesis of TiO_2/Co/carbon nanofibers with tunable and efficient electromagnetic absorption. *Chem Eng J* 2020, **380**: 122591.
[40] Liu ZW, Mahale P, Engels EA. Sepsis and risk of cancer among elderly adults in the United States. *Clin Infect Dis* 2019, **68**: 717–724.
[41] Zhang XX, Cheng XT, Si Y, *et al.* Elastic and highly fatigue resistant ZrO_2–SiO_2 nanofibrous aerogel with low energy dissipation for thermal insulation. *Chem Eng J* 2022, **433**: 133628.
[42] Han ZP, Wang JQ, Liu SP, *et al.* Electrospinning of neat graphene nanofibers. *Adv Fiber Mater* 2022, **4**: 268–279.
[43] Cao XY, Deng JP, Pan K. Electrospinning Janus type CoO_x/C nanofibers as electrocatalysts for oxygen reduction reaction. *Adv Fiber Mater* 2020, **2**: 85–92.
[44] Zhao YJ, Zhang YN, Yang CR, *et al.* Ultralight and flexible SiC nanoparticle-decorated carbon nanofiber mats for broad-band microwave absorption. *Carbon* 2021, **171**: 474–483.
[45] Zhao JY, Li ZL, Lv SW, *et al.* Electrospun advanced nanomaterials for *in situ* transmission electron microscopy: Progress and perspectives. *InfoMat* 2023, **5**: e12483.
[46] Zhou XD, Zhang HB, Yuan MY, *et al.* Dispersing magnetic nanoparticles into staggered, porous nano-frameworks: Weaving and visualizing nanoscale magnetic flux lines for enhanced electromagnetic absorption. *Adv Funct Mater* 2024: 2314541.
[47] Liu QH, Cao Q, Bi H, *et al.* CoNi@SiO_2@TiO_2 and CoNi@air@TiO_2 microspheres with strong wideband microwave absorption. *Adv Mater* 2016, **28**: 486–490.
[48] Xia T, Zhang C, Oyler NA, *et al.* Hydrogenated TiO_2 nanocrystals: A novel microwave absorbing material. *Adv Mater* 2013, **25**: 6905–6910.
[49] Huang ZY, Chen HH, Huang Y, *et al.* Ultra-broadband wide-angle terahertz absorption properties of 3D graphene foam. *Adv Funct Mater* 2018, **28**: 1704363.
[50] Guo YY, Zhang M, Chen TT, *et al.* Enhancing electromagnetic wave absorption in carbon fiber using FeS_2 nanoparticles. *Chem Eng J* 2023, **16**: 9591–9601.
[51] Qiu JF, Peng CY, Wang RC, *et al.* One-step *in-situ* preparation of C/TiO_2@rGO aerogel derived from $Ti_3C_2T_x$ MXene for integrating microwave absorption, electromagnetic interference shielding and catalytic degradation of antibiotics. *Carbon* 2024, **217**: 118610.
[52] Duan Y, Yu ZY, Hu SJ, *et al.* Scaled-up synthesis of amorphous NiFeMo oxides and their rapid surface reconstruction for superior oxygen evolution catalysis. *Angew Chem Int Ed* 2019, **58**: 15772–15777.
[53] Lv HL, Yang ZH, Liu B, *et al.* A flexible electromagnetic wave-electricity harvester. *Nat Commun* 2021, **12**: 834.
[54] Zhang X, Qiao J, Wang FL, *et al.* Tailoring electromagnetic absorption performances of TiO_2/Co/carbon nanofibers through tuning graphitization degrees. *Ceram Int* 2020, **46**: 4754–4761.
[55] Fesenko O, Dovbeshko G, Dementjev A, *et al.* Graphene-enhanced Raman spectroscopy of thymine adsorbed on single-layer graphene. *Nanoscale Res Lett* 2015, **10**: 163.
[56] Lou ZC, Wang QY, Zhang Y, *et al.* *In-situ* formation of low-dimensional, magnetic core–shell nanocrystal for electromagnetic dissipation. *Compos Part B Eng* 2021, **214**: 108744.
[57] Chen F, Zhang SS, Ma BB, *et al.* Bimetallic CoFe–MOF@$Ti_3C_2T_x$ MXene derived composites for broadband microwave absorption. *Chem Eng J* 2022, **431**: 134007.
[58] Wang ZC, Pei K, Yang LT, *et al.* Topological spin texture in the

pseudogap phase of a high-T_C superconductor. *Nature* 2023, **615**: 405–410.
[59] He J, Han MJ, Wen K, *et al.* Absorption-dominated electromagnetic interference shielding assembled composites based on modular design with infrared camouflage and response switching. *Compos Sci Technol* 2023, **231**: 109799.
[60] Li X, Wang L, You WB, *et al.* Enhanced polarization from flexible hierarchical MnO_2 arrays on cotton cloth with excellent microwave absorption. *Nanoscale* 2019, **11**: 13269–13281.
[61] Liang HS, Liu JL, Zhang Y, *et al.* Ultra-thin broccoli-like SCFs@TiO_2 one-dimensional electromagnetic wave absorbing material. *Compos Part B Eng* 2019, **178**: 107507.
[62] Yuan MY, Zhao B, Yang CD, *et al.* Remarkable magnetic exchange coupling via constructing Bi-magnetic interface for broadband lower-frequency microwave absorption. *Adv Funct Mater* 2022, **32**: 2203161.
[63] Chen GY, Zhang RX, Yuan MY, *et al.* Visualizing nanoscale interlayer magnetic interactions and unconventional low-frequency behaviors in ferromagnetic multishelled structures. *Adv Mater* 2024, **36**: 2313411.
[64] Yang JJ, Wang JQ, Li HQ, *et al.* MoS_2/MXene aerogel with conformal heterogeneous interfaces tailored by atomic layer deposition for tunable microwave absorption. *Adv Sci* 2022, **9**: e2101988.
[65] Pan YL, Zhu QQ, Zhu JH, *et al.* Macroscopic electromagnetic synergy network-enhanced N-doped Ni/C gigahertz microwave absorber with regulable microtopography. *Nano Res* 2023, **16**: 10666–10677.
[66] Zhao ZH, Zhang LM, Wu HJ. Hydro/organo/ionogels: "controllable" electromagnetic wave absorbers. *Adv Mater* 2022, **34**: 2205376.
[67] Qiao J, Zhang X, Liu C, *et al.* Facile fabrication of Ni embedded TiO_2/C core–shell ternary nanofibers with multicomponent functional synergy for efficient electromagnetic wave absorption. *Compos Part B Eng* 2020, **200**: 108343.
[68] Li X, Hu RZ, Xiong ZQ, *et al.* Metal-organic gel leading to customized magnetic-coupling engineering in carbon aerogels for excellent radar stealth and thermal insulation performances. *Nano-Micro Lett* 2023, **16**: 42.
[69] Liu XY, Ma WL, Qiu ZR, *et al.* Manipulation of impedance matching toward 3D-printed lightweight and stiff MXene-based aerogels for consecutive multiband tunable electromagnetic wave absorption. *ACS Nano* 2023, **17**: 8420–8432.
[70] Huang WH, Song M, Wang S, *et al.* Dual-step redox engineering of 2D CoNi-alloy embedded B, N-doped carbon layers toward tunable electromagnetic wave absorption and light-weight infrared stealth heat insulation devices. *Adv Mater* 2024, **36**: 2403322.
[71] Hou Y, Quan J, Su XR, *et al.* Carbonized silk fiber mat: A flexible and broadband microwave absorber, and the length effect. *ACS Sustain Chem Eng* 2021, **9**: 12747–12754.
[72] Wu ZC, Cheng HW, Jin C, *et al.* Dimensional design and core–shell engineering of nanomaterials for electromagnetic wave absorption. *Adv Mater* 2022, **34**: 2107538.
[73] Hou Y, Quan J, Thai BQ, *et al.* Ultralight biomass-derived carbon fibre aerogels for electromagnetic and acoustic noise mitigation. *J Mater Chem A* 2022, **10**: 22771–22780.
[74] Cheng XT, Chang XY, Liao YL, *et al.* Highly compressible and stretchable ceramic aerogels with nanofiber-nanosheet binary synergistic structure for thermal insulation in extreme environments. *Ceram Int* 2024, **50**: 7451–7457.
[75] Wu F, Qiang SY, Zhang XH, *et al.* The rising of flexible and elastic ceramic fiber materials: Fundamental concept, design principle, and toughening mechanism. *Adv Funct Mater* 2022, **32**: 2207130.
[76] Qin GY, Huang XX, Yan X, *et al.* Carbonized wood with ordered channels decorated by $NiCo_2O_4$ for lightweight and high-performance microwave absorber. *J Adv Ceram* 2022, **11**: 105–119.
[77] Cao MS, Wang XX, Zhang M, *et al.* Electromagnetic response and energy conversion for functions and devices in low-dimensional materials. *Adv Funct Mater* 2019, **29**: 1807398.
[78] Li SZ, Cheng XT, Han GT, *et al.* Elastic and compressible Al_2O_3/ZrO_2/La_2O_3 nanofibrous membranes for firefighting protective clothing. *J Colloid Interf Sci* 2023, **636**: 83–89.